



# Novel Thoracic MRI Approaches for the Assessment of Pulmonary Physiology and Inflammation

Jonathan P. Brooke and Ian P. Hall

## Abstract

Excessive pulmonary inflammation can lead to damage of lung tissue, airway remodelling and established structural lung disease. Novel therapeutics that specifically target inflammatory pathways are becoming increasingly common in clinical practice, but there is yet to be a similar stepwise change in pulmonary diagnostic tools. A variety of thoracic magnetic resonance imaging (MRI) tools are currently in development, which may soon fulfil this emerging clinical need for highly sensitive assessments of lung structure and function. Given conventional MRI techniques are poorly suited to lung imaging, alternate strategies have been developed, including the use of inhaled contrast agents, intravenous contrast and specialized lung MR sequences. In this chapter, we discuss technical challenges of performing MRI of the lungs and how they may be overcome. Key thoracic MRI modalities are reviewed, namely, hyperpolarized noble gas MRI, oxygen-enhanced MRI (OE-MRI), ultrashort echo time (UTE) MRI and dynamic contrast-enhanced (DCE)

MRI. Finally, we consider potential clinical applications of these techniques including phenotyping of lung disease, evaluation of novel pulmonary therapeutic efficacy and longitudinal assessment of specific patient groups.

## Keywords

Thoracic MRI · Hyperpolarized gas · Helium-3 · Xenon-129 · Oxygen-enhanced MRI · Ultrashort echo time · Dynamic contrast-enhanced MRI

## Abbreviations

$^{129}\text{Xe}$	Xenon-129
$^3\text{He}$	Helium-3
ADC	Apparent diffusion coefficient
ASL	Arterial spin labelling
BOS	Bronchiolitis obliterans syndrome
CF	Cystic fibrosis
CFTR	Cystic fibrosis transmembrane receptor
COPD	Chronic obstructive pulmonary disease
CT	Computed tomography
CTPA	CT pulmonary angiography
DCE	Dynamic contrast enhancement
$D_{\text{LCO}}$	Diffusion capacity of the lung for carbon dioxide
DPD	Dynamic proton density

J. P. Brooke (✉) · I. P. Hall (✉)  
Department of Respiratory Medicine, University of Nottingham, Queens Medical Centre, Nottingham, UK  
e-mail: [jonathan.brooke@nottingham.ac.uk](mailto:jonathan.brooke@nottingham.ac.uk); [ian.hall@nottingham.ac.uk](mailto:ian.hall@nottingham.ac.uk)

DWI	Diffusion-weighted imaging
FEV <sub>1</sub>	Forced expiratory volume in 1 second
GRE	Gradient recall echo
ILD	Interstitial lung disease
IPF	Idiopathic pulmonary fibrosis
LAM	Lymphangiomyomatosis
LCI	Lung clearance index
LVR	Lung volume reduction
MRA	Magnetic resonance angiography
MRI	Magnetic resonance imaging
OE-MRI	Oxygen-enhanced MRI
OTF	Oxygen transfer function
PE	Pulmonary embolism
PET	Positron emission tomography
PFT	Pulmonary function test
RBC	Red blood cell
RER	Relative enhancement ratio
RF	Radiofrequency
SS	Systemic sclerosis
SUV <sub>max</sub>	Maximum standardized uptake value
T	Tesla
UTE	Ultrashort echo time
V/Q	Ventilation-perfusion
VDP	Ventilation defect percentage
VDV	Ventilation defect volume
ZTE	Zero echo time

## 8.1 Introduction

Inflammation dictates much of the discrete repertoire of responses the lungs employ against injury. Sophisticated filtration, removal and immune-mediated pulmonary defences work in parallel to limit entry of pathogens and environmental particulates. When initial defences are overwhelmed, a vigorous acute inflammatory response confines and destroys noxious agents and promotes recovery [1]. An extreme manifestation of this response is the acute respiratory distress syndrome, in which an exaggerated inflammatory cascade disrupts the alveolar-capillary membrane, leading to severe respiratory failure [2]. Persistence of acute inflammation may be followed by a chronic inflammatory response designed to clear necrotic tissue, isolate

remaining infective organisms and repair damaged lung. Abnormal chronic inflammation is implicated in many lung diseases, including asthma, chronic obstructive pulmonary disease (COPD), cystic fibrosis (CF) and interstitial lung disease (ILD). In these conditions, chronic inflammation can lead to progressive tissue damage, airway remodelling or established structural lung disease [3–5]. The location and mechanism (including immune cell and cytokine expression) of this inflammation vary, which gives rise to distinct patterns of lung disease.

Novel pulmonary therapeutics such as biologics and cystic fibrosis transmembrane receptor (CFTR) modulators can modify abnormal and excessive inflammation, either by targeting an element of the inflammatory pathway or indirectly downregulating its activity. These therapies mark a paradigm shift in lung disease management towards precision medicine and personalized care, but there is yet to be a similar stepwise change in diagnostic tools.

Conventional respiratory diagnostics include blood tests, pulmonary function tests (PFTs) and a range of thoracic imaging. While the plain radiograph remains a key screening and diagnostic investigation, it is frequently complemented by several other modalities including ultrasound, computed tomography (CT), positron emission tomography (PET) and ventilation-perfusion (V/Q) imaging. CT remains the gold standard for assessment of lung structure and is tremendously versatile as a diagnostic tool for parenchymal lung disease, pulmonary vascular disorders, malignancy and pulmonary infection. The demand for CT imaging in healthcare is continually growing, and developments such as low-dose CT screening for lung cancer will likely see this increase further [6]. However, CT has limited scope for functional assessment, and while PFTs offer a global assessment of airflow, lung volumes and gas transfer, they are insensitive to regionally heterogeneous lung disease.

Although unlikely to replace CT, the novel thoracic magnetic resonance imaging (MRI) approaches discussed in this chapter may offer highly sensitive assessments of regionally heterogeneous lung disease that complement existing

diagnostics. The absence of ionizing radiation also provides a new avenue for longitudinal imaging, which could be useful for the detection of early lung disease progression and evaluation of therapeutic interventions.

## 8.2 Basic Principles of MRI

MRI is widely used in clinical medicine, most notably for neuro-, cardiac, vascular, soft tissue and abdominal imaging. Standard images are acquired by exploiting the magnetic ‘spin’ property of protons in hydrogen atoms, applying a complex series of magnetic fields and then using radiofrequency (RF) pulses to localize and characterize those protons in a target tissue [7].

### The MRI Scanner

The MR signals used to create an image are generated by a series of magnetic coils contained within the housing of the MRI scanner (Fig. 8.1). The main magnetic coil is a superconducting

magnet cooled to approximately  $-269\text{ }^{\circ}\text{C}$  using cryogenic liquid helium. At this temperature, resistance to the flow of electric current is minimal. Thus, a high electric current flowing through the coil’s loops of wire creates a high-strength magnetic field orientated in the z-axis. This strong magnetic field is referred to as  $B_0$  and its field strength is measured in Tesla (T) units [8]. Clinical MRI scanners generally employ 1.5 or 3 T fields, but ultra-high-field scanners up to 11.7 T are currently in development for future research in human subjects [9].

Gradient coils create a secondary magnetic field that distorts  $B_0$  in orthogonal directions. Most MR systems employ three sets of gradient coils, one for each orthogonal plane – x, y and z. The primary function of these coils is spatial encoding of MR signals. Shim coils also adjust  $B_0$ , but their purpose is to increase magnetic field homogeneity. This action minimizes local susceptibility effects (e.g. due to a person lying in the scanner) that would otherwise disrupt  $B_0$  field homogeneity and degrade image quality.

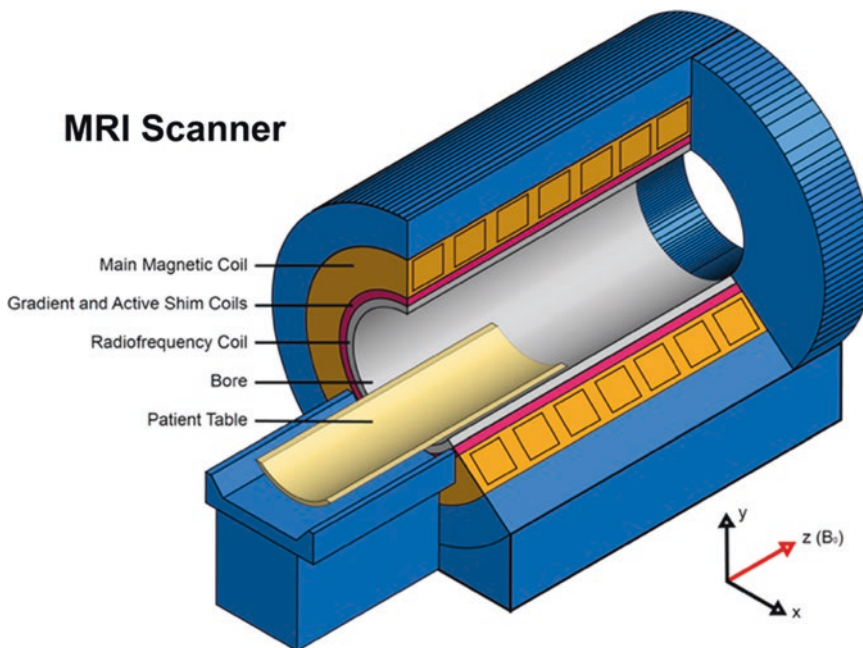


**Fig. 8.1** Cross section of an MRI scanner. A closed bore MRI scanner is shown. A concentric series of magnet coils surrounds the bore of the scanner. The main magnetic field ( $B_0$ ) is orientated in the z-axis, parallel to the

scanner’s bore. A sliding table allows a subject to be moved into and out of the scanner. (Adapted from Introduction to neuroimaging analysis [10])

RF coils transmit RF energy and detect proton RF signals. Some RF coils only transmit or receive, whereas others can do both. The transmit coil generates an RF pulse of electromagnetic energy that alters the spin of protons in  $B_0$ . When the RF pulse is switched off, protons create their own RF signal, which the receive coil can detect. The RF coil magnetic field is called  $B_1$ .

The sum of  $B_1$ ,  $B_0$  and gradient coil magnetic fields is a spatially localized output signal which is detected by the receive RF coil. Complex computer algorithms encode these output signals as volume elements (voxels) which are combined to create an MRI [8].

### Basic MRI Physics

The following is an abbreviated explanation of MRI physics, which can be expanded upon with the literature referenced in this section.

The magnetic susceptibility of hydrogen and its abundance within the body are fundamental to conventional MRI. The atomic nucleus of hydrogen consists of a single positively charged proton that spins on its axis. This spinning proton generates a small magnetic field perpendicular to the direction of spin called a 'magnetic moment' [8]. When placed in the strong magnetic field of an MRI scanner, these magnetic moments become aligned to  $B_0$ . Most protons stay in a low energy state lining up parallel to  $B_0$ , but the remainder occupy a high energy state and instead line up anti-parallel to  $B_0$ . This results in protons having a net longitudinal magnetization parallel to  $B_0$  [11, 12]. When in  $B_0$ , the spin axis of a proton is altered in a similar fashion to gravity acting upon a spinning top. The rotational motion of this spin axis is called precession. The resonance element of MRI occurs when an RF pulse is applied at the same frequency as the precession rate of these protons in a given magnetic field [13].

When an RF pulse is applied, some protons are flipped from a low to a high energy state, which reduces longitudinal magnetization. Proton spins are also pushed together so they precess in phase. The result is a net transverse magnetization vector relative to  $B_0$  called a flip angle [7].

After the RF pulse is turned off, two types of proton relaxation effect can be measured. T1

relaxation occurs when high energy protons relax into the low energy state, release heat and restore longitudinal magnetization parallel to  $B_0$ . T2 relaxation occurs when the positively charged protons repel one another and no longer precess in phase [7]. Tissues in the human body exhibit characteristic differences in T1 and T2 relaxation dependent upon the quantity of hydrogen they contain and the molecular structure of hydrogen containing compounds. This allows for contrast between different tissues and anatomical structures to be detected on an MRI scan.

Greater contrast can be achieved by altering RF pulses or delivering multiple RF pulses in a so-called pulse sequence. Underpinning these concepts are two key MRI parameters: echo time and repetition time. Echo time is the time between delivery of an RF pulse and sampling of the resultant proton MR signal. Repetition time is the duration of one pulse sequence. Adjustment of these parameters can emphasize T1 and T2 relaxation effects resulting in T1- or T2-weighted images [14].

The eventual MRI is comprised of voxels, which represent the location and relative magnetic signal of protons in the scanned tissue. Voxels are conventionally displayed in grayscale, and their brightness varies based on MR signal strength: the stronger the signal, the brighter the voxel. MR signals are localized by gradient coils that apply a magnetic gradient to a slice of tissue and then encode the orthogonal position of protons by adjusting precession frequency (frequency encoding) and precession phase (phase encoding). A composite MR signal is then generated, which is initially stored as K-space data. After MRI acquisition, Fourier transformation is performed by computer software to convert the raw K-space data into an image [12, 15].

---

## 8.3 Technical Challenges of Thoracic MRI

MRI has advanced significantly since 1977 when the first in vivo human imaging of a finger and the thorax were performed [16, 17]. Despite this historical starting point, the lungs have been

somewhat of an orphan organ amongst the otherwise extensive use of MRI in contemporary medical care. Instead, CT has been dominant in thoracic imaging given its affordability, speed and ease of interpretation [18]. Modern CT imaging rapidly delivers localized structural data and protocol improvements have significantly reduced ionizing radiation doses without compromising image quality [19]. As such, MRI is perhaps best thought of as a complement to, rather than a replacement for, current thoracic imaging methods. However, the difficulties of applying conventional MRI techniques to the lungs have been a hindrance to its mass adoption. The fundamental issues with performing MRI of the lungs are:

- Low tissue density
- Numerous air-tissue interfaces
- Physiological motion of the heart and thoracic cavity

MRI typically relies on protons in the target tissue to generate an MR signal. Lungs have a relatively low density, with a combined mass of approximately 1 kg in a thoracic volume of 4–5 L for a typical adult [20]. As such, lung proton density is significantly lower than that of other solid organs, which leads to reduced MR signal. Signal is further attenuated by magnetic susceptibility artefact due to the millions of air-tissue interfaces in the lower respiratory tract. These interfaces cause substantial local magnetic field inhomogeneity with rapid loss of proton MR signal during imaging [21]. The result is lung that appears uniformly black and featureless on standard MRI. Third, the physiological motion of the heart and thoracic cavity can produce ghost images and further artefact during MR acquisition, which also degrade image quality [22]. The key strategies used to tackle these issues are:

- Use of intravenous or inhaled contrast agents
- Implementation of specialized lung MR sequences
- Respiratory and cardiac gating

Intravenous gadolinium contrast is widely used for clinical MRI scans, notably in vascular and neuroimaging. Its ability to shorten T1 relaxation creates greater contrast between tissues, and thus pathology can be more easily identified

[23]. While this is helpful for pulmonary vascular imaging, the approach does not appreciably improve lung parenchymal images. Instead, lung MRI has seen a predominant focus on inhaled contrast agents such as hyperpolarized noble gases, oxygen and more recently fluorinated hydrocarbons. These substances generate an inherently higher MR signal than the lung itself and facilitate visualization of the airways alongside functional information concerning flow, ventilation and gas exchange [24].

For structural imaging, specialized sequences have been designed to overcome the rapid signal decay that inhibits the use of conventional MRI in the lungs. These sequences minimize so-called echo time, which allows lung MR signal to be acquired before decay occurs. Ultrashort and zero echo time (UTE and ZTE) sequences employ this principle and can produce images of lung parenchyma comparable to CT [25].

Finally, thoracic motion can be addressed in a few ways. For short sequences, a single breath hold may suffice, but longer sequences typically require gating. Respiratory gating allows the subject to free breathe and can be achieved during imaging with an external sensor or belt worn by the subject set to trigger acquisition at the same point in each respiratory cycle [26]. Alternatively, respiratory navigated sequences that identify the diaphragm and automatically trigger acquisition when the diaphragm is in a specified imaging window can be used [27]. ECG gating may also be used to control for cardiac motion, but this significantly prolongs examination time and is probably a lesser priority than control of respiratory motion [28]. All of these methods also assume control of extra-thoracic motion, and as such, subjects must remain as still as possible during an imaging sequence.

---

## 8.4 Thoracic MRI Modalities

### 8.4.1 Overview of Hyperpolarized Gas MRI

As discussed, the lungs are an inherently challenging organ to image with conventional MRI



techniques. An inhaled noble gas was one of the first solutions as demonstrated by Albert et al. in 1994, using hyperpolarized xenon-129 ( $^{129}\text{Xe}$ ) to image ex vivo mouse lungs [29]. Compared with lung, the inherently greater signal of the hyperpolarized gas allowed the airways to be visualized, and this work was soon translated in vivo to human subjects in 1997 by Mugler et al. [30].

A close competitor for  $^{129}\text{Xe}$  was another noble gas: helium-3 ( $^3\text{He}$ ). The first hyperpolarized  $^3\text{He}$  images were acquired in guinea pig lungs by Middleton et al., with an improved MR signal when compared to the  $^{129}\text{Xe}$  images from 1 year before [31].  $^3\text{He}$  then became the favoured hyperpolarized gas in thoracic MRI for many years, as polarization methods and imaging quality were superior. However, scarcity and expense when compared to  $^{129}\text{Xe}$  has seen  $^3\text{He}$  use decline more recently.

A number of adjustments to conventional MRI are required for hyperpolarized gas imaging. First, a polarizer is needed to manufacture hyperpolarized gas by means of spin exchange optical pumping. The scanner itself must also be calibrated for resonance of the noble gases, given the gyromagnetic ratios, and hence Larmor frequencies of  $^{129}\text{Xe}$  and  $^3\text{He}$  differ from that of a proton. Finally, a dedicated radiofrequency (RF) coil, again attuned to the appropriate frequency, is necessary for an image to be generated [32]. While some of this equipment is commercially available, many research teams have developed their own bespoke polarizers and coils instead.

#### 8.4.2 Hyperpolarized $^3\text{He}$ MRI

$^3\text{He}$  is an inert gas, and unlike the more abundant  $^4\text{He}$  isotope, the odd number of nucleons (two protons and one neutron) facilitates the magnetic spin required for MRI. Early adoption in thoracic MRI was facilitated by sophisticated hyperpolarization techniques, allowing levels of polarization of around 30%, compared with 1–2% for  $^{129}\text{Xe}$  [33]. This equated to superior MR signal and image quality, which placed  $^3\text{He}$  as the front-runner in hyperpolarized gas MRI research for many years. However,  $^3\text{He}$  used in medical

research is derived from the radioactive decay of tritium (hydrogen-3), a substance historically used in the manufacture of nuclear weapons. In recent years, the supply of tritium has dwindled, which has made use of  $^3\text{He}$  prohibitive and prompted a move back towards  $^{129}\text{Xe}$  [34].

$^3\text{He}$  imaging is typically performed during a breath hold, where hyperpolarized  $^3\text{He}$  rapidly diffuses through the airways and remains confined in the lungs. Given its insolubility in lung tissue, side effects are uncommon (~6–7% of subjects) and often mild, for example a self-limiting cough or dry mouth [35]. The inhaled  $^3\text{He}$  mixture is typically anoxic, and so modest oxygen desaturation (~4%) may be observed, but recovery is usually rapid upon free breathing of room air [36]. An anoxic mixture delays loss of polarity by limiting  $^3\text{He}$  interaction with paramagnetic oxygen. However, once inhaled,  $^3\text{He}$  undergoes rapid depolarization, both due to its interaction with oxygen in the airways and the application of RF pulses during imaging [37]. This rapid loss of polarity, alongside the constraint of a single breath hold, means images need to be obtained within approximately 20 seconds. Given the MRI scanner and RF coil are specifically attuned to  $^3\text{He}$ , the resulting image isolates structures that contain the hyperpolarized gas – in this case, the airways – and excludes the surrounding tissues [38].

#### Static Ventilation $^3\text{He}$ Imaging

In static ventilation imaging, ventilation heterogeneity is localized and quantified during a  $^3\text{He}$  breath hold. Areas of decreased  $^3\text{He}$  signal imply a reduction in ventilation, referred to as ventilation defects. These are typically described as the ventilation defect volume (VDV) or ventilation defect percentage (VDP), which are regionally mapped and quantitative measures of pulmonary ventilation [39].

One of the earliest uses of hyperpolarized  $^3\text{He}$  in human subjects by Kauczor et al. demonstrated ventilation defects in a spectrum of lung diseases. Defects were visible in patients with COPD, bronchiectasis, lung cancer and pleural effusion and correlated well with pathology visible on conventional imaging [40]. Mathew et al. showed defects

in COPD patients varied little for same-day imaging, but changed more after a 1-week interval, despite stable spirometry [41]. As perhaps would be expected, similar studies in asthma have shown ventilation defects can be induced by exercise and methacholine challenge [42] and improve with inhaled beta-agonist administration [43]. More interestingly, longitudinal studies in asthma have shown defects may persist or recur in the same locations, which is thought to reflect areas of chronic inflammation and airway remodelling [44]. Small ventilation defects can also be seen in healthy patients with normal lung function, and these should not be mistaken as pathological during image analysis [45].

In CF, ventilation defects correlate with forced expiratory volume in 1 second ( $FEV_1$ ) but are also seen in patients with normal range spirometry (Fig. 8.2) [46]. While studies with chest physiotherapy and nebulized DNase have shown little change in global measures of  $^3\text{He}$  ventilation, regional differences before and after treatment can be detected, which may represent shifting airway secretions [46, 47]. Altes et al. demonstrated ventilation defects decrease in patients with G551D mutation taking ivacaftor, but return to baseline after washout of the drug. Improvements were even seen in patients with normal range spirometry and those with small changes in  $FEV_1$ , which supports the potential role of hyperpolarized gas MRI as a sensitive biomarker [48].

### Diffusion-Weighted $^3\text{He}$ Imaging

Diffusion-weighted imaging (DWI) in conventional MRI assesses the net diffusion of water molecules in tissues [49]. This technique is commonly used in neuroimaging to identify restricted diffusion as seen in acute ischaemic stroke, malignancy and white matter disease [50]. DWI lung MRI instead measures the diffusion of hyperpolarized gas through the airways.  $^3\text{He}$  DWI is performed during a breath hold, and diffusion is quantified as the apparent diffusion coefficient (ADC). ADC is a relative measure of diffusion restriction and can be represented visually as an ADC map to compare regions of interest [51].

ADC characteristically reduces as airway calibre decreases. This is well demonstrated in healthy lungs where ADC in the major airways is higher, and lower but homogeneous in peripheral airways [52]. In contrast, small airway destruction causes foci of increased ADC as seen in emphysematous lung (Fig. 8.3) [53]. Subclinical lung disease can also be detected, with even very mild emphysematous change demonstrating increased ADC values [54]. In COPD, mean ADC is well correlated with diffusion capacity of the lung for carbon monoxide ( $D_{LCO}$ ), reinforcing the role of ADC as a surrogate marker of alveolar damage [55]. ADC also shows greater sensitivity than spirometry to detect deterioration in lung function of COPD patients over periods of up to 2 years [56].

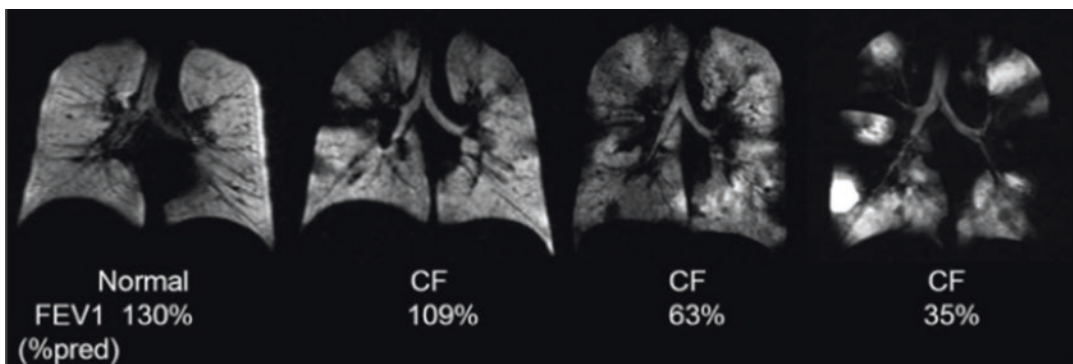


**Fig. 8.2**  $^3\text{He}$  MRI of static ventilation in CF. Comparison of a healthy subject and three adults with CF. An increasing burden of ventilation defects is demonstrated with

deteriorating lung function [46]. (Image reproduced with permission of the rights holder. Elsevier – License number: 4858760327184)

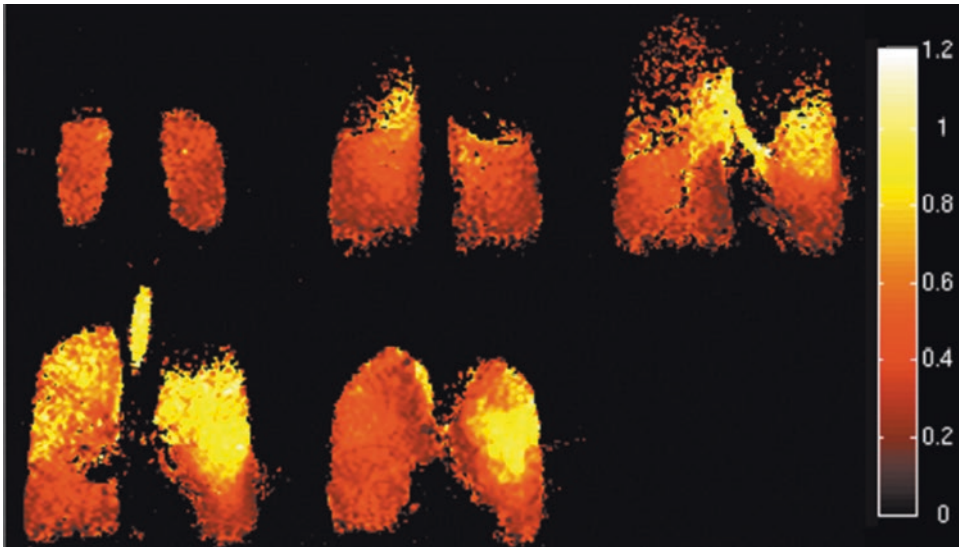


**Fig. 8.3**  $^3\text{He}$  MRI ADC map in severe COPD. Coronal views of a patient with severe COPD show increased ADC values (yellow pixels) in both upper lobes in keeping with emphysematous lung. Similar ADC values are also seen in

large calibre airways (trachea and main bronchi). Coloured bar units are  $\text{cm}^2/\text{second}$  [53]. (Image reproduced with permission of the rights holder. John Wiley and Sons – License number: 4858820929850)

In idiopathic pulmonary fibrosis (IPF), mean ADC is also increased as damaged alveoli lose surface area and  $^3\text{He}$  diffusion becomes less restricted [57]. Chan et al. showed mean ADC correlates with  $D_{\text{LCO}}$  and CT fibrosis scores and used an alternate DWI metric – the derived mean diffusive length scale – which estimates the mean alveolar dimension in a voxel [58] to demonstrate DWI is sensitive to small changes in IPF lung morphometry over a 1-year period [57].

### 8.4.3 Hyperpolarized $^{129}\text{Xe}$ MRI

In contrast to  $^3\text{He}$ , xenon is lipophilic, making it readily soluble in pulmonary tissues as well as the bloodstream. This property is key to its anaesthetic effect but also the basis of dissolved phase MR imaging [30]. Approximately 2% of inhaled xenon dissolves, leaving ample gas for airspace MR signal [34]. The  $^{129}\text{Xe}$  isotope used in hyperpolarized MRI is conveniently abundant, comprising roughly a quarter of naturally occurring xenon derived from the atmosphere [32].  $^{129}\text{Xe}$  imaging has demonstrated an excellent safety profile in both healthy volunteers and patients

with various lung diseases [59]. Common side effects include tingling, dizziness and euphoria, which are invariably mild and short-lived [60].

Many of the techniques developed for  $^3\text{He}$  MRI have been applied to  $^{129}\text{Xe}$  including ventilation and DWI.  $^{129}\text{Xe}$ 's solubility in pulmonary tissues has also led to great interest in dissolved phase imaging. As such, the use of  $^{129}\text{Xe}$  MRI has grown considerably over the past decade as a virtue of favourable economics, better polarization technology and its scope for unique and sensitive functional lung imaging [34].

#### Static Ventilation $^{129}\text{Xe}$ Imaging

When the transition of hyperpolarized gas MRI from  $^3\text{He}$  to  $^{129}\text{Xe}$  began, various research groups sought to compare the two modalities. In 2010, Altes et al. showed the imaging quality of both was comparable, and similar ventilation defects could be detected in healthy volunteers and patients with COPD, asthma and CF [61]. However, subsequent work by other groups has highlighted important differences between  $^3\text{He}$  and  $^{129}\text{Xe}$  static ventilation imaging.

An intriguing finding was that some ventilation defects are seemingly missed or ‘masked’



with  $^3\text{He}$  when compared side by side to  $^{129}\text{Xe}$  imaging [62]. This was reflected by greater  $^{129}\text{Xe}$  VDP in COPD [62] and asthma [63] compared to  $^3\text{He}$ . Svenningsen et al. investigated asthmatic patients who had previously undergone  $^3\text{He}$  imaging after methacholine challenge [64] with repeat  $^3\text{He}$  and  $^{129}\text{Xe}$  imaging 1 year later. They found that follow-up  $^{129}\text{Xe}$  imaging without provocation testing revealed defects that had previously only been detectable with  $^3\text{He}$  once methacholine had been given (Fig. 8.4) [63].

The rationale behind this may be the lower diffusion coefficient and higher density of  $^{129}\text{Xe}$ , which results in its slower airway transit and delayed filling of poorly ventilated lung [62, 63]. Gas mixtures using  $^{129}\text{Xe}$  are typically closer in density to air; hence, their diffusion coefficients are similar. This similarity allows clinically relevant ventilation defects to be visualized with  $^{129}\text{Xe}$ , which may otherwise be undetectable with  $^3\text{He}$  [62].

Static ventilation studies with  $^{129}\text{Xe}$  have otherwise explored similar lung diseases to  $^3\text{He}$ . In COPD,  $^{129}\text{Xe}$  ventilation correlates with functional measures including spirometry [62] and V/Q imaging [65]. Ventilation defects improve after beta-agonist use in asthma [63] and may be a more sensitive measure than spirometry to detect lung function decline with advancing age [66]. Elevated VDP and ventilation heterogeneity have been shown in CF subjects with even mild lung disease ( $\text{FEV}_1 \geq 100\%$ ) [67], and  $^{129}\text{Xe}$  defects correlate with lung clearance index (LCI) in this

group [68]. In lymphangioleiomyomatosis (LAM), co-registered  $^{129}\text{Xe}$  and CT images have also shown significant ventilation heterogeneity between similarly sized cystic lung volumes, which highlights the merit of combining functional images alongside conventional structural assessments [69].

#### Diffusion-Weighted $^{129}\text{Xe}$ Imaging

The majority of  $^{129}\text{Xe}$  DWI research has been conducted in COPD, where  $^3\text{He}$  and  $^{129}\text{Xe}$  ADC measurements have shown good correlation with one another [62]. When compared to  $^3\text{He}$ , absolute  $^{129}\text{Xe}$  ADC values are smaller [70], which likely reflects xenon's lower diffusion coefficient as described previously.

$^{129}\text{Xe}$  ADC correlates with emphysematous burden and alveolar destruction on both CT [71] and ex vivo histological samples [72]. Various groups have also shown strong correlations with spirometry and  $D_{\text{LCO}}$  measurements. Research in other lung diseases has been more limited, but  $^{129}\text{Xe}$  ADC measurements have been successfully performed in CF [73], LAM [69] and ex vivo IPF lungs [72].

#### Dissolved Phase $^{129}\text{Xe}$ Imaging

Dissolved phase  $^{129}\text{Xe}$  MR takes advantage of xenon's solubility in pulmonary tissue to generate quantifiable and spatially localized gas exchange imaging. Xenon follows the same transfer pathway as oxygen, diffusing through the alveolar-capillary unit and then transiently

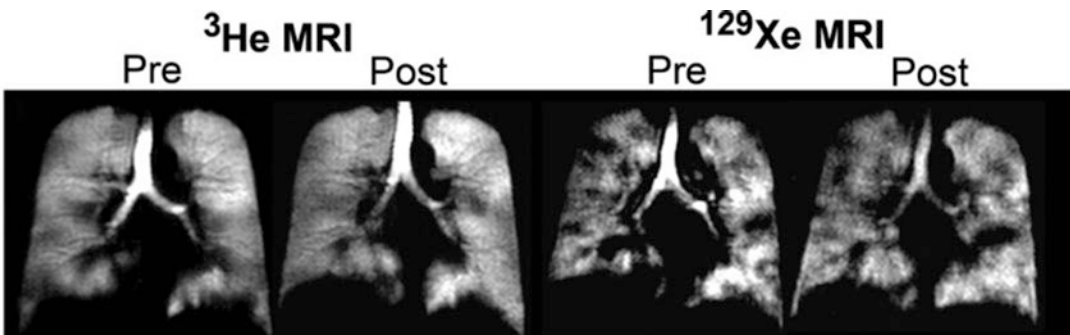


**Fig. 8.4** Comparison of  $^3\text{He}$  and  $^{129}\text{Xe}$  static ventilation MRI in a subject with asthma. Coronal views of a patient with asthma taken pre- and post-bronchodilator.  $^{129}\text{Xe}$  MRI reveals ventilation defects that are not detected with

$^3\text{He}$  [63]. (Image reproduced with permission of the rights holder. John Wiley and Sons – License number: 4858821365032)

binding with haemoglobin once in the bloodstream [74]. A chemical shift relative to the gaseous phase occurs when  $^{129}\text{Xe}$  diffuses into the pulmonary interstitium (referred to as ‘barrier tissues’ in dissolved phase imaging) and again upon diffusion into red blood cells (RBCs). Due to chemical shift, each compartment has a distinct  $^{129}\text{Xe}$  MR signal – gas, barrier and RBC – that can be detected by selective excitation of the appropriate  $^{129}\text{Xe}$  resonant frequency [75].

Early attempts to acquire a dissolved phase image were hampered by low  $^{129}\text{Xe}$  polarization levels and poor MR signal [30]. In contrast to the gas phase, relatively little  $^{129}\text{Xe}$  dissolves into barrier tissues (roughly 2%), and once there MR signal degrades rapidly [75]. These problems were overcome with frequency-selective RF pulses to isolate a combined barrier/RBC dissolved phase signal sufficient to create an image. These initial studies in healthy volunteers showed a dissolved phase gradient, where MR signal increases in the dependent lung. This is thought to represent increased perfusion and alveolar compression of those areas during imaging [75].

Later studies refined the technique further to generate separate barrier and RBC dissolved phase images [74]. This has allowed better discrimination of the gas exchange mechanics in lung pathology, with a particular focus on ILD. In IPF, Kaushik et al. showed mean RBC signal was decreased and barrier signal increased when compared with healthy controls. This results in a low RBC : barrier ratio which strongly correlates with  $D_{\text{LCO}}$  [74]. Low RBC/barrier ratio is also seen in COPD, again correlating with  $D_{\text{LCO}}$  as well as CT emphysema score [76] (Fig. 8.5).

Regional mapping has helped identify three patterns of impaired gas exchange in the dissolved phase imaging of IPF. These are thought to represent different levels of disease activity, which are [78]:

1. Diffusion block – high barrier and low RBC signal
2. End stage fibrosis – low/normal barrier and low RBC signal
3. Early/active disease – high barrier and normal RBC signal

While the ‘end stage fibrosis’ pattern overlaps with areas of severe fibrosis on CT, the ‘early/active disease’ pattern lacks such change on conventional imaging. Given a single MRI voxel contains upwards of 40,000 alveoli, these areas may represent early disease that could be used as a functional MR biomarker of inflammation [78]. Finally, recent work with higher field strength MRI has shown the sensitivity of dissolved phase  $^{129}\text{Xe}$  can be augmented further to provide greater imaging resolution in IPF as well as other lung diseases [79].

#### 8.4.4 Oxygen-Enhanced MRI (OE-MRI)

Oxygen can also be used as an MR contrast agent in oxygen-enhanced MRI (OE-MRI). However, unlike hyperpolarized gases, oxygen itself is not directly visualized. Instead, the weakly paramagnetic molecular oxygen ( $\text{O}_2$ ) shortens T1 relaxation in lung tissue and the pulmonary circulation during MRI. When 100% oxygen is inhaled, T1 relaxation is shortened by approximately 9% [80], leading to a rise in T1-weighted signal.

Oxygen transport in the lungs is dependent upon ventilation, diffusion and perfusion, such that the T1-weighted signal in OE-MRI is representative of all three processes. It follows that disruption to any of these elements in lung pathology can then affect the oxygen-enhanced signal [81]. Maximal T1 signal is obtained when alveolar capillary blood is saturated with molecular oxygen, and Mai et al. demonstrated this could be achieved with an oxygen flow rate of 15 L/min [82]. Flow rates above this do not increase T1 signal further; hence, OE-MRI sequences typically employ sequential room air and 15 L/min acquisitions.

OE-MRI is typically performed during free breathing with acquisitions taking several minutes to complete. To improve image quality and reduce movement artefact, respiratory gating with navigator echoes that identify the diaphragm during imaging can be used [83]. High-flow oxygen and face masks are inexpensive and widely available, which means there are few barriers to performing

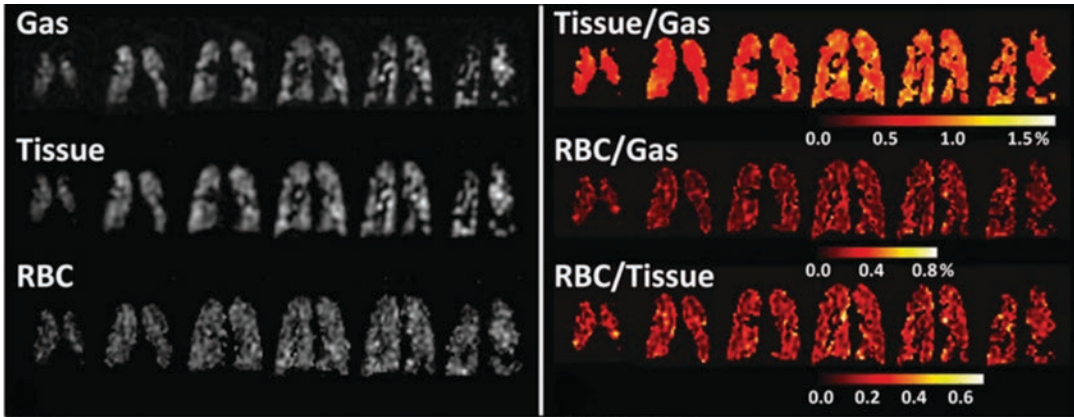


**Fig. 8.5**  $^{129}\text{Xe}$  dissolved phase MRI in severe COPD. Coronal views of the three  $^{129}\text{Xe}$  phases and ratio maps in one subject. A large number of ventilation defects are seen in the gas phase. There is also marked heteroge-

neity of the dissolved phase and ratio maps [77]. (Image reproduced with permission of the rights holder. John Wiley and Sons – License number: 4858830024322)

OE-MRI with standard clinical MRI scanners. However, MR signal is relatively small when compared to hyperpolarized gases and oxygen itself can alter pulmonary physiology [80]. Data from OE-MRI can be displayed and quantified in several ways, including T1 mapping and calculation of relative enhancement or oxygen transfer. In addition, OE-MRI may also be combined with intravenous gadolinium for V/Q imaging.

### T1 Mapping in OE-MRI

T1 maps are one method of visualizing OE-MRI data and are typically colour-coded to represent different T1 relaxations (Fig. 8.6). Images performed with different fractions of inspired oxygen ( $\text{FiO}_2$ ) can then be compared for qualitative evaluation of lung function. In healthy subjects, 100% oxygen causes widespread reduction of T1 relaxation with some heterogeneity [81]. The T1 maps in lung disease are generally even more heterogeneous and exhibit lower T1 relaxation values due to impaired oxygen transport [84].

Renne et al. demonstrated heterogeneity of T1 maps in lung transplant recipients with bronchiolitis obliterans syndrome (BOS), but median T1 relaxation values could not discriminate between stages of disease [86]. However, other studies have verified the regional sensitivity of lung T1 measurement. Jakob et al. identified focal lung

disease in CF that exhibited both blunted T1 relaxation and matched perfusion abnormality [87]. Similar findings have also been shown in patients with CF receiving nebulized hypertonic saline [88].

### Relative Enhancement and Oxygen Transfer Function

To help describe and visualize regional lung function in OE-MRI quantitatively, the terms relative enhancement ratio (RER) and oxygen transfer function (OTF) have been developed. First, RER describes the change in T1 signal intensity of spatially matched voxels between room air and 100% oxygen images [89]. It can be represented visually as a relative enhancement map or alternatively several regions of interest can be identified and the RER for each one calculated. Ohno et al. used these methods to show markedly lower RER in patients with lung cancer and emphysema compared with healthy volunteers. This study also showed that mean RER strongly correlated with  $\text{FEV}_1$  and  $D_{\text{LCO}}$  [89]. The same research group has since corroborated these findings in a larger cohort of COPD patients [90] and found similar but weaker correlations in patients with asthma [91] and ILD [92].

OE-MRI VDP can also be derived from RER and has shown strong correlation of  $^3\text{He}$  VDP



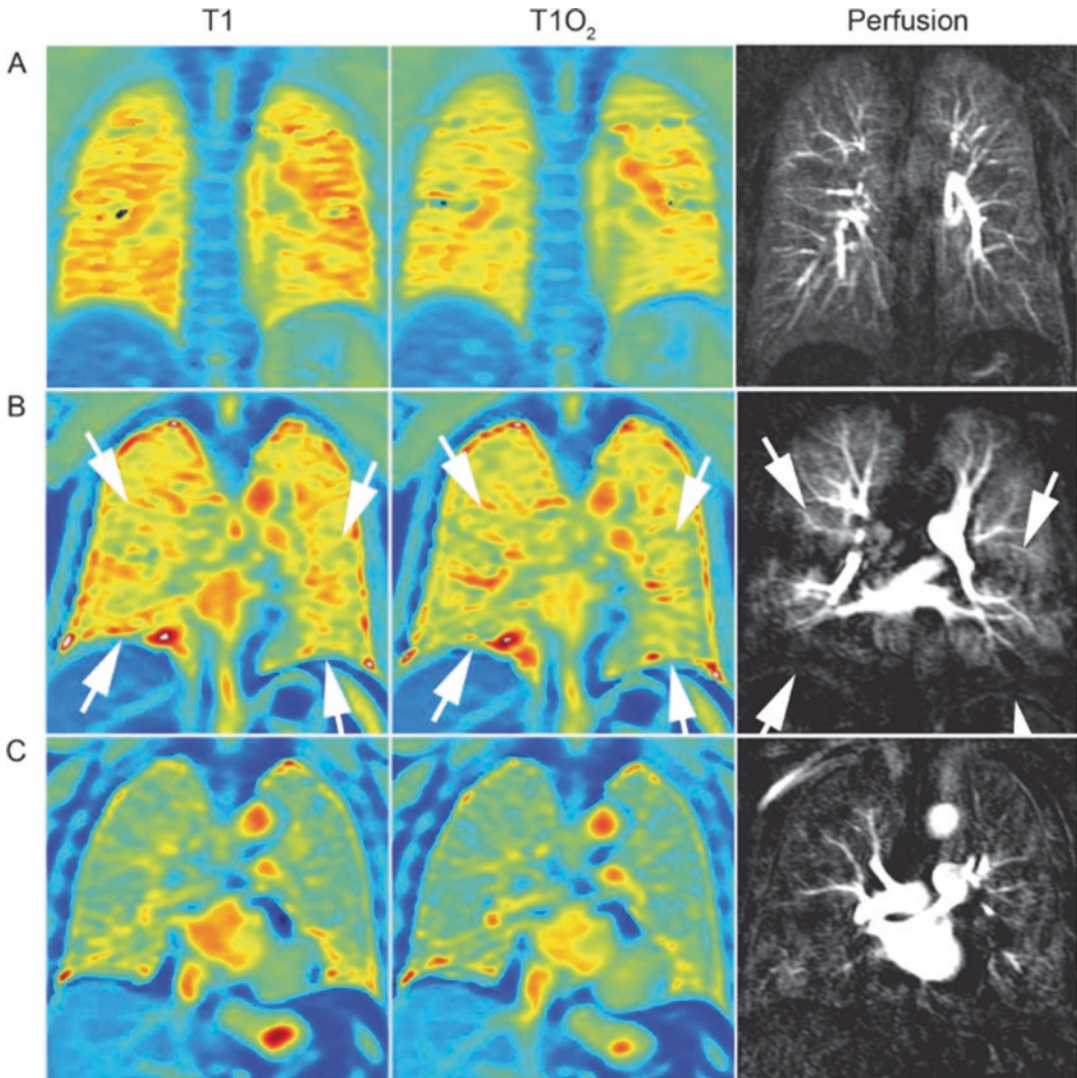


**Fig. 8.6** OE-MRI T1 maps and DCE perfusion MRI. Coronal views of three subjects: (a) healthy subject, (b) and (c) COPD. Reduction in oxygen-enhanced signal with 100% oxygen (T1O<sub>2</sub>). Signal is significantly diminished in COPD subjects. Minor ventilation and perfusion

abnormalities are demonstrated in subject b (white arrows). More marked abnormalities are seen in subject c [85]. (Image reproduced under Creative Commons Attribution License)

measurements in adults with CF. However, OE-MRI VDP measures were approximately 5% lower than <sup>3</sup>He VDP [93]. This likely reflects key differences in the performance of these techniques as OE-MRI has a longer wash-in time and lower spatial resolution and measures a combination of ventilation, diffusion and perfusion as previously discussed.

OTF describes the change in lung T1 relaxation rate (R1) for a given oxygen concentration and represents a combination of airflow, oxygen diffusion and lung perfusion [86, 87]. In the original paper, adults with CF showed significant OTF heterogeneity and areas of poor oxygen transfer also demonstrated MR perfusion abnormalities [87]. Renne et al. later examined the effect of endoscopic allergen testing on OTF and

airway eosinophil count in asthma. Their study showed OTF decreased in airway segments exposed to allergen, with a corresponding airway eosinophilia. Follow-up MRI after 24 hours showed OTF then returned to baseline [94]. The same research group has also measured OTF in lung allograft recipients finding it is significantly lower in patients with evidence of BOS [86].

### Ventilation/Perfusion OE-MRI

V/Q imaging was part of the inception of OE-MRI in 1996. Edelman et al. compared gadolinium-based perfusion imaging alongside oxygen-enhanced ventilation images to demonstrate V/Q mismatch [95]. In patients with COPD, oxygen enhancement is also markedly abnormal and strongly correlated with perfusion abnormalities [85].

Arterial spin labelling (ASL) has been used as alternative measure of perfusion for V/Q imaging in combination with OE-MRI. ASL precludes the need for an injected contrast agent and instead uses magnetically labelled arterial blood as a tracer [96]. In healthy volunteers, V/Q imaging has been successfully performed using this method, including the demonstration of a matched V/Q defect in a subject following left upper lobectomy [97].

### 8.4.5 Ultrashort Echo Time (UTE) MRI

Ultrashort echo time (UTE) is a proton-based MRI modality and was first described by Bergin et al. as a means of obtaining structural lung images [98]. This is achieved by minimizing the delay between application of an RF pulse and detection of the resulting MR signal. The resulting UTE images were comparable to CT of the time.

Given the rapid decay of lung MR signal during MRI, the echo time for UTE is by necessity  $\leq 200 \mu\text{s}$  [21]. So-called zero echo time (ZTE) sequences reduce this further to as little as  $5 \mu\text{s}$ , but the exact echo time achievable is limited by the software and hardware constraints of the MR platform used [99].

Typically, UTE sequences also employ specialized radial sampling approaches to acquire imaging data, which contrast with the Cartesian sampling methods used for conventional MRI [100]. This method helps to minimize motion artefact and facilitate free-breathing scans through respiratory gating [101]. Recent UTE techniques with self-gating discard any motion-corrupted data and use the remaining data to create the final images [102]. The result is a signal-averaged MRI scan with improved resolution by virtue of the pooled imaging data [103].

### UTE MRI for Assessment of Structural Lung Disease

Neonatal intensive care patients are particularly prone to pulmonary morbidity due to prolonged periods of oxygen therapy and mechanical ventilation. Self-gated UTE can produce CT-like images in these patients by controlling for bulk movement and respiratory motion without the need for sedation [104]. In this way, end-inspiratory and -expiratory images can estimate tidal volume and identify structural lung change in bronchopulmonary dysplasia (BPD) [102, 105]. In BPD, preliminary studies have suggested UTE can be used to quantify hyperinflation to predict clinical outcomes, and could be used for longitudinal follow-up [104, 105].

In infants with CF, UTE has demonstrated good correlation with CT for bronchiectasis and bronchial wall thickening [106]. Similar structural imaging has also been demonstrated in adults with CF using free-breathing UTE acquisitions lasting 8–15 minutes (Fig. 8.7) [107].

In COPD, UTE shows short-term reproducibility over a 3-week period [108] and can produce structural information comparable to CT [109]. Chassagnon et al. compared a cohort of systemic sclerosis (SS) patients with and without evidence of ILD on CT. In this study, elastic registration of inspiratory and expiratory UTE showed increased lung stiffness in patients with SS-related ILD, corresponding with areas of fibrosis on HRCT [110].

UTE has also shown promising results in the detection and morphological characterization of lung nodules. Studies have shown UTE can detect



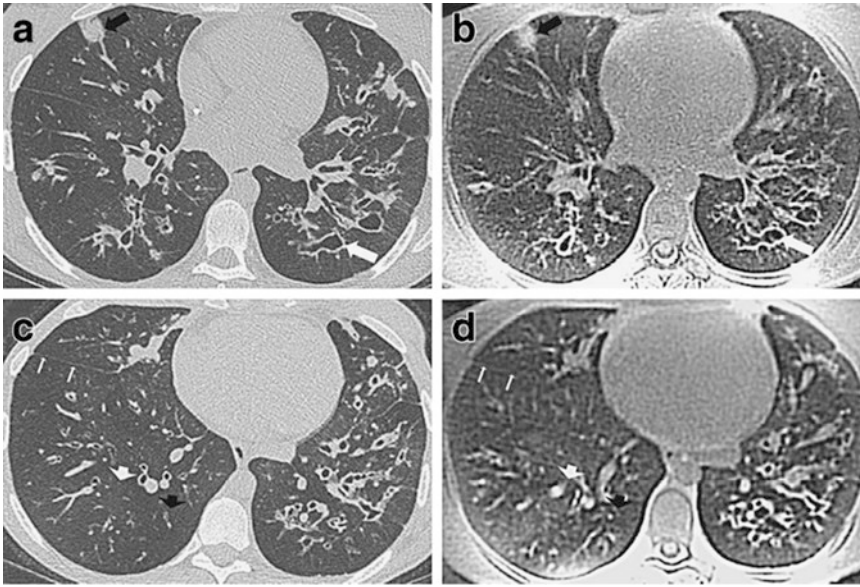


**Fig. 8.7** Axial CT and UTE MRI in an adolescent with CF. CT (**a, c**) and UTE MRI (**b, d**) slices show evidence of nodular consolidation (black arrow in **a** and **b**) and wide-

spread bronchiectatic change [107]. (Image reproduced with permission of the rights holder. Springer Nature – License number: 4858830473723)

between 73% and 86% of nodules when compared to CT, but is markedly less sensitive for identification of very small modules (i.e. those <4 mm) [111, 112]. It also tends to underestimate long- and short-axis nodule measurements by up to 1–2 mm [113].

#### UTE MRI for Assessment of Lung Function

UTE is an appealing foundation for co-registered structural and functional lung MRI as it is capable of reducing acquisition times and capturing motion-insensitive images during free breathing.

Sheikh et al. demonstrated a variation of UTE imaging – dynamic proton density (DPD) – in healthy volunteers and patients with asthma, comparing them to hyperpolarized  $^3\text{He}$  MRI. Breath hold UTE images were acquired and used to generate DPD maps that reflect the difference in UTE signal intensity between full inspiration and expiration. This technique demonstrated ventilation heterogeneity and produced functional data comparable to  $^3\text{He}$  imaging in patients given methacholine and salbutamol [114].

UTE can also be combined with inhaled contrast agents such as  $^{129}\text{Xe}$  and oxygen to augment

pulmonary assessment. For  $^{129}\text{Xe}$  MRI, UTE sequences can improve image resolution and decrease breath hold times when compared to the conventionally used gradient recall echo (GRE) sequences [115]. Shortened T1 relaxation time in the presence of 100% oxygen also makes UTE desirable for OE-MRI and allows whole lung acquisitions with isotropic resolution in as little as 5 minutes alongside simultaneous structural imaging [116].

#### 8.4.6 Dynamic Contrast-Enhanced MRI

Dynamic contrast-enhanced (DCE) MRI uses gadolinium-based intravenous contrast agents for pulmonary imaging. As discussed previously, gadolinium shortens T1 relaxation, which creates contrast between imaged tissues [23]. While this is less helpful for imaging lung parenchyma (given T1 relaxation values are already very short), gadolinium is well suited to pulmonary vascular imaging and can be used to evaluate abnormal lesions through measurement of changes in perfusion and vascular permeability.

### **Pulmonary Vascular Imaging with Gadolinium**

MR angiography (MRA) with gadolinium can be used to evaluate acute and chronic pulmonary vascular disease. For the diagnosis of chronic thromboembolic pulmonary hypertension, the performance of MRA is comparable to CT angiography, but the extent of disease is still better characterized with CT [117]. The use of MRA in pulmonary embolism (PE) has historically been less successful; the multicentre PIOPED III study found a quarter of MR images were inadequate and overall 43% of PEs were missed [118]. A later study by Schiebler et al. significantly improved on this, with 97.4% of scans of diagnostic quality and a 1-year negative predictive value of 97% for PE [119]. In clinical practice, MRA may yet become a suitable alternative to CT pulmonary angiography (CTPA) when radiation exposure and iodinated contrast agents need to be avoided.

### **Assessment of Parenchymal Lung Disease with DCE MRI**

DCE MRI may be used to evaluate inflammatory activity and characterize severity of ILD. Chin et al. measured time to peak contrast enhancement after gadolinium injection in ILD patients and correlated these findings with imaging-targeted lung biopsies [120]. Areas found to be inflammatory predominant on biopsy were characterized by early contrast enhancement, whereas fibrotic-predominant areas displayed late enhancement. More recently, Buzan et al. compared peak contrast enhancement with disease severity (assessed instead by CT) in a mixed group of ILD patients [121]. They found non-IPF patients had earlier peak enhancement than the IPF cohort, but only in the non-IPF group could severity of lung disease be discriminated by time to peak enhancement. These findings may represent different vascularity at the histological level, whereby less severe or actively inflamed lesions in ILD demonstrate greater vascularization and permeability to contrast. Conversely, severely fibrotic areas in IPF have low vascularity and hence delayed contrast enhancement. These inferences are similar to those encountered with

dissolved phase  $^{129}\text{Xe}$  MRI [78], and so DCE MRI may present an alternate avenue for assessment of lung disease activity and response to pulmonary therapeutics in ILD.

In children with CF, early detection of lung disease may also be possible with DCE MRI. Amaxopoulou et al. demonstrated a spectrum of perfusion deficits despite normal appearances of lung parenchyma on structural imaging [122]. This is likely a reflection of small airways disease that would otherwise not be detectable with standard imaging. Kellenberger et al. also measured perfusion abnormalities in a mixed cohort of paediatric patients with congenital thoracic malformations [123]. At peak enhancement, perfusion deficits were evident in areas of hyperinflation, cystic malformation, bronchopulmonary sequestration and bronchogenic cysts. Both studies show DCE MRI can add highly sensitive functional data to proton-density imaging, which together provide a comprehensive assessment of complex thoracic abnormalities in the paediatric population.

### **Assessment of Pulmonary Nodules and Malignancy with DCE MRI**

Complex pharmacokinetic parameters of gadolinium enhancement in pulmonary nodules and lung cancers have been explored by several groups as a means of differentiating benign and malignant aetiologies. Ohno et al. found DCE MRI measures of perfusion were comparable to the PET-CT maximum standardized uptake value ( $\text{SUV}_{\text{max}}$ ) in the differentiation of solitary pulmonary nodules [124]. Other groups have also suggested a role for DCE MRI in the risk stratification of malignancy, notably for evaluation of radiologically indeterminate lesions [125, 126].

DCE MRI biomarkers have also been evaluated as potential predictors of anti-cancer therapy. Huang et al. found DCE MRI-derived markers of tumour perfusion and vascular permeability ( $K_{\text{trans}}$  and  $K_{\text{ep}}$ ) were correlated with both  $\text{SUV}_{\text{max}}$  and decreased tumour size in lung cancer patients 6 weeks after radiotherapy [127]. Xu et al. similarly found that after 1 week of chemotherapy, tumour  $K_{\text{trans}}$  and  $K_{\text{ep}}$  decreased significantly in lung cancer patients defined later as treatment

responders according to conventional CT criteria [128]. As such, these MR imaging-based biomarkers could offer sensitive early measures of treatment response to complement existing imaging techniques.

## 8.5 The Potential Role of Thoracic MRI in Respiratory Medicine

At present, the thoracic MRI modalities discussed in this chapter are predominantly used as research tools. Clinical translation of these techniques is a complex matter and requires technical hurdles to be addressed alongside consideration of application and health economics. For certain modalities, such as hyperpolarized gas MRI, their cost and technical requirements will likely be prohibitive for some institutions. Instead, delivery by specialist tertiary centres may be more feasible. It is then important to consider how these imaging techniques can answer key research questions and complement existing clinical methods of assessing lung structure and function.

One of the most often cited advantages of thoracic MRI is the absence of ionizing radiation. X-ray-based investigations can deliver substantial radiation doses, and so their use should be carefully rationalized by clinicians. The stewardship of ionizing radiation is particularly relevant in the following situations:

- For patients with long-term/lifelong conditions who may require serial imaging
- The investigation of thromboembolic disease in pregnancy, where radiation exposure to the breast tissue may increase future cancer risk [129]
- When minimizing radiation exposure is essential, such as in ataxia-telangiectasia where faulty DNA repair mechanisms greatly increase lifetime cancer risk [130]

However, potential limitations of thoracic MRI must also be considered as some techniques may be particularly challenging for certain patients:

- Modalities requiring prolonged scanning time may be uncomfortable for younger patients or

patients who struggle to lie flat for extended periods due to breathlessness.

- Patients with significant breathlessness or cough may also find breath hold manoeuvres difficult during techniques like hyperpolarized gas MRI.
- Inhalation of anoxic contrast agents (viz.  $^3\text{He}$  and  $^{129}\text{Xe}$ ) may be unsuitable in patients with severe lung disease due to risk of hypoxia.
- Some inhaled contrast agents can also cause sedation:  $^{129}\text{Xe}$  is known to have anaesthetic effects [131], and high-flow oxygen can precipitate hypercapnic respiratory failure in susceptible patients [132].

Therefore, wider use of thoracic MRI requires evaluation of both its merits and its clinical practicality. As highlighted previously, there are some discrete situations where techniques such as UTE MRI or MRA could be the preferred imaging method for specific patient groups. However, the complete replacement of conventional studies that use ionizing radiation remains impractical given the current demands and financial models of healthcare [133].

### Phenotyping Lung Disease with Thoracic MRI

Some thoracic MRI research has focused on the phenotyping of airways disease, namely in asthma and COPD. Increasingly, different asthma phenotypes are recognized, which has allowed treatments such as biologics to be tailored to the individual patient [134]. Phenotyping of asthma with MRI shows promise and highlights some of the difficulties encountered in the assessment of asthma severity. Hyperpolarized gas MRI can demonstrate regional ventilation defects, and while correlation with disease severity and spirometry is observed, some patients have marked ventilation defects in the presence of preserved spirometry [135]. When compared to other measurements such as CT and provocation testing, ventilation defects can also be indicative of regional airway remodelling [136]. Therefore, MRI may be particularly interesting when its findings are discordant with standard diagnostic tools like spirometry.

Historically, COPD has been divided into emphysematous and chronic bronchitis pheno-

types, but broader classification based on anatomical, physiological or pathophysiological criteria has been suggested [137]. Some of these patterns of disease can be demonstrated using MRI, which could then be used to guide therapy. One example is lung volume reduction (LVR), given the increasing use of endobronchial valves. Patient selection for LVR is key, with favourable outcomes often linked to upper lobe predominant emphysema [138]. However, valve insertion in lower lobe predominant emphysema has also proven useful when collateral ventilation is minimal [139]. Hyperpolarized  $^3\text{He}$  MRI has been used retrospectively to identify alternate targets for endobronchial valve insertion undetected on CT. In theory, this may increase the number of patients to whom LVR could be offered, but further research is required [140].  $^3\text{He}$  MRI has also been used to detect bronchodilator response [141] and identify patients with the ‘frequent exacerbator’ phenotype [142], but these applications would likely be harder to justify in clinical practice.

### Assessing Response to Novel Therapeutics

It has been established that evidence of lung disease can be detected in patients with CF who have normal spirometry using MRI and lung clearance index (LCI) [143, 144]. As such, traditional measures like  $\text{FEV}_1$  may lack the sensitivity required for future clinical practice and research trials. Instead, thoracic MRI using hyperpolarized gases or non-contrast functional measures could serve as imaging-based biomarkers to evaluate therapies like CFTR modulators and aid longitudinal monitoring of lung disease [48, 145].

As discussed previously, hyperpolarized  $^{129}\text{Xe}$  and DCE MRI methods may become useful in assessing different levels of disease activity in ILD [78, 121]. In particular, functional imaging with hyperpolarized  $^{129}\text{Xe}$  demonstrates longitudinal deterioration of gas exchange in IPF with a greater sensitivity than transfer factor ( $D_{\text{LCO}}$ ) [146]. In this way, early detection of lung disease progression could be feasible and become an invaluable tool for the evaluation of novel therapeutics.

## 8.6 Conclusion

There have been tremendous advances in thoracic MRI since the pioneering hyperpolarized gas and structural imaging studies of the mid-1990s. However, widespread adoption is yet to be realized with CT remaining the workhorse of cross-sectional lung imaging in clinical practice.

Structural imaging without ionizing radiation already has clear clinical applications, but further refinements to improve spatial resolution are needed to bridge the gap between thoracic MRI and CT. Functional imaging shows tremendous promise, and we can expect this to become increasingly relevant in the delivery of cutting-edge medical therapies that require highly sensitive measures of lung function.

Substantial work is still required for clinical translation, but the potential of co-registered structural and functional imaging without ionizing radiation is an exciting prospect for the future of respiratory care.

## References

1. Moldoveanu B, Otmishi P, Jani P, Walker J, Sarmiento X, Guardiola J, et al. Inflammatory mechanisms in the lung. *J Inflamm Res*. 2009;2:1–11.
2. Sweeney RM, McAuley DF. Acute respiratory distress syndrome. *Lancet*. 2016;388(10058):2416–30.
3. James AL, Wenzel S. Clinical relevance of airway remodelling in airway diseases. *Eur Respir J*. 2007;30(1):134–55.
4. Cottin V, Hirani NA, Hotchkiss DL, Nambiar AM, Ogura T, Otaola M, et al. Presentation, diagnosis and clinical course of the spectrum of progressive-fibrosing interstitial lung diseases. *Eur Respir Rev*. 2018;27(150):180076.
5. Cantin AM, Hartl D, Konstan MW, Chmiel JF. Inflammation in cystic fibrosis lung disease: pathogenesis and therapy. *J Cyst Fibros*. 2015;14(4):419–30.
6. Oudkerk M, Devaraj A, Vliegenthart R, Henzler T, Prosch H, Heussel CP, et al. European position statement on lung cancer screening. *Lancet Oncol*. 2017;18(12):e754–e66.
7. Pooley RA. Fundamental physics of MR imaging. *Radiographics*. 2005;25(4):1087–99.
8. Currie S, Hoggard N, Craven IJ, Hadjivassiliou M, Wilkinson ID. Understanding MRI: basic MR physics for physicians. *Postgrad Med J*. 2013;89(1050):209–23.



9. Ertürk MA, Wu X, Eryaman Y, Van de Moortele P-F, Auerbach EJ, Lagore RL, et al. Toward imaging the body at 10.5 tesla. *Magn Reson Med*. 2017;77(1):434–43.
10. Jenkinson M, Chappell M. *Introduction to neuroimaging analysis*. New York: Oxford University Press; 2018.
11. Grover VPB, Tognarelli JM, Crossey MME, Cox IJ, Taylor-Robinson SD, McPhail MJW. Magnetic resonance imaging: principles and techniques: lessons for clinicians. *J Clin Exp Hepatol*. 2015;5(3):246–55.
12. Sands MJ, Levitin A. Basics of magnetic resonance imaging. *Semin Vasc Surg*. 2004;17(2):66–82.
13. Westbrook C. In: Westbrook C, Roth CK, Talbot JM, editors. *MRI in practice*. 4th ed. Oxford: Wiley-Blackwell; 2011.
14. Nitz WR, Reimer P. Contrast mechanisms in MR imaging. *Eur Radiol*. 1999;9(6):1032–46.
15. Vassiliou VS, Cameron D, Prasad SK, Gatehouse PD. Magnetic resonance imaging: physics basics for the cardiologist. *JRSM Cardiovasc Dis*. 2018;7:2048004018772237.
16. Mansfield P, Maudsley AA. Medical imaging by NMR. *Br J Radiol*. 1977;50(591):188–94.
17. Damadian R, Goldsmith M, Minkoff L. NMR in cancer: XVI. FONAR image of the live human body. *Physiol Chem Phys*. 1977;9(1):97–100, 108.
18. Iezzi R, Larici AR, Franchi P, Marano R, Magarelli N, Posa A, et al. Tailoring protocols for chest CT applications: when and how? *Diagn Interv Radiol (Ankara, Turkey)*. 2017;23(6):420–7.
19. Thakur Y, McLaughlin PD, Mayo JR. Strategies for radiation dose optimization. *Curr Radiol Rep*. 2013;1(1):1–10.
20. Gustafsson T, Eriksson A, Wingren CJ. Multivariate linear regression modelling of lung weight in 24,056 Swedish medico-legal autopsy cases. *J Forensic Legal Med*. 2017;46:20–2.
21. Torres L, Kammerman J, Hahn AD, Zha W, Nagle SK, Johnson K, et al. Structure-function imaging of lung disease using ultrashort echo time MRI. *Acad Radiol*. 2019;26(3):431–41.
22. Kauczor HU, Kreitner KF. MRI of the pulmonary parenchyma. *Eur Radiol*. 1999;9(9):1755–64.
23. Lipton ML. In: Lipton ML, editor. *Totally accessible MRI: a user's guide to principles, technology, and applications*. New York: Springer; 2008.
24. Kruger SJ, Nagle SK, Couch MJ, Ohno Y, Albert M, Fain SB. Functional imaging of the lungs with gas agents. *J Magn Reson Imaging: JMIRI*. 2016;43(2):295–315.
25. Wild JM, Marshall H, Bock M, Schad LR, Jakob PM, Puderbach M, et al. MRI of the lung (1/3): methods. *Insights Imaging*. 2012;3(4):345–53.
26. Johnson KM, Fain SB, Schiebler ML, Nagle S. Optimized 3D ultrashort echo time pulmonary MRI. *Magn Reson Med*. 2013;70(5):1241–50.
27. Oechsner M, Pracht ED, Staeb D, Arnold JFT, Köstler H, Hahn D, et al. Lung imaging under free-breathing conditions. *Magn Reson Med*. 2009;61(3):723–7.
28. Raptis CA, Ludwig DR, Hammer MM, Luna A, Broncano J, Henry TS, et al. Building blocks for thoracic MRI: challenges, sequences, and protocol design. *J Magn Reson Imaging: JMIRI*. 2019;50:682–701.
29. Albert MS, Cates GD, Driehuys B, Happer W, Saam B, Springer CS, et al. Biological magnetic resonance imaging using laser-polarized  $^{129}\text{Xe}$ . *Nature*. 1994;370(6486):199–201.
30. Mugler JP III, Driehuys B, Brookeman JR, Cates GD, Berr SS, Bryant RG, et al. MR imaging and spectroscopy using hyperpolarized  $^{129}\text{Xe}$  gas: preliminary human results. *Magn Reson Med*. 1997;37(6):809–15.
31. Middleton H, Black RD, Saam B, Cates GD, Cofer GP, Guenther R, et al. MR imaging with hyperpolarized  $^3\text{He}$  gas. *Magn Reson Med*. 1995;33(2):271–5.
32. Mugler JP III, Altes TA. Hyperpolarized  $^{129}\text{Xe}$  MRI of the human lung. *J Magn Reson Imaging*. 2013;37(2):313–31.
33. Roos JE, McAdams HP, Kaushik SS, Driehuys B. Hyperpolarized gas MR imaging: technique and applications. *Magn Reson Imaging Clin N Am*. 2015;23(2):217–29.
34. Ebner L, Kammerman J, Driehuys B, Schiebler ML, Cadman RV, Fain SB. The role of hyperpolarized ( $^{129}\text{Xe}$ ) in MR imaging of pulmonary function. *Eur J Radiol*. 2017;86:343–52.
35. Altes T, Gersbach J, Mata J, Mugler III J, Brookeman J, de Lange E, editors. Evaluation of the safety of hyperpolarized helium-3 gas as an inhaled contrast agent for MRI. In: *Proceedings of the Fifteenth Meeting of the International Society for Magnetic Resonance in Medicine Berkeley, CA: International Society for Magnetic Resonance in Medicine; 2007*.
36. Lutey BA, Lefrak SS, Woods JC, Tanoli T, Quirk JD, Bashir A, et al. Hyperpolarized  $^3\text{He}$  MR imaging: physiologic monitoring observations and safety considerations in 100 consecutive subjects. *Radiology*. 2008;248(2):655–61.
37. Wild JM, Paley MNJ, Viallon M, Schreiber WG, van Beek EJ, Griffiths PD. k-Space filtering in 2D gradient-echo breath-hold hyperpolarized  $^3\text{He}$  MRI: spatial resolution and signal-to-noise ratio considerations. *Magn Reson Med*. 2002;47(4):687–95.
38. Altes TA, de Lange EE. Applications of hyperpolarized helium-3 gas magnetic resonance imaging in pediatric lung disease. *Top Magn Reson Imaging: TMRI*. 2003;14(3):231–6.
39. Fain S, Schiebler ML, McCormack DG, Parraga G. Imaging of lung function using hyperpolarized helium-3 magnetic resonance imaging: review of current and emerging translational methods and applications. *J Magn Reson Imaging: JMIRI*. 2010;32(6):1398–408.



40. Kauczor HU, Ebert M, Kreitner KF, Nilgens H, Surkau R, Heil W, et al. Imaging of the lungs using  $^3\text{He}$  MRI: preliminary clinical experience in 18 patients with and without lung disease. *J Magn Reson Imaging: JMRI*. 1997;7(3):538–43.
41. Mathew L, Evans A, Ouriadov A, Etemad-Rezai R, Fogel R, Santyr G, et al. Hyperpolarized  $^3\text{He}$  magnetic resonance imaging of chronic obstructive pulmonary disease: reproducibility at 3.0 tesla. *Acad Radiol*. 2008;15(10):1298–311.
42. Samee S, Altes T, Powers P, de Lange EE, Knight-Scott J, Rakes G, et al. Imaging the lungs in asthmatic patients by using hyperpolarized helium-3 magnetic resonance: assessment of response to methacholine and exercise challenge. *J Allergy Clin Immunol*. 2003;111(6):1205–11.
43. Altes TA, Powers PL, Knight-Scott J, Rakes G, Platts-Mills TA, de Lange EE, et al. Hyperpolarized  $^3\text{He}$  MR lung ventilation imaging in asthmatics: preliminary findings. *J Magn Reson Imaging: JMRI*. 2001;13(3):378–84.
44. de Lange EE, Altes TA, Patrie JT, Battiston JJ, Juersivich AP, Mugler JP 3rd, et al. Changes in regional airflow obstruction over time in the lungs of patients with asthma: evaluation with  $^3\text{He}$  MR imaging. *Radiology*. 2009;250(2):567–75.
45. Lee EY, Sun Y, Zurakowski D, Hatabu H, Khatwa U, Albert MS. Hyperpolarized  $^3\text{He}$  MR imaging of the lung: normal range of ventilation defects and PFT correlation in young adults. *J Thorac Imaging*. 2009;24(2):110–4.
46. Mentore K, Froh DK, de Lange EE, Brookeman JR, Paget-Brown AO, Altes TA. Hyperpolarized HHe 3 MRI of the lung in cystic fibrosis: assessment at baseline and after bronchodilator and airway clearance treatment. *Acad Radiol*. 2005;12(11):1423–9.
47. Woodhouse N, Wild JM, van Beek EJ, Hoggard N, Barker N, Taylor CJ. Assessment of hyperpolarized  $^3\text{He}$  lung MRI for regional evaluation of interventional therapy: a pilot study in pediatric cystic fibrosis. *J Magn Reson Imaging: JMRI*. 2009;30(5):981–8.
48. Altes TA, Johnson M, Fidler M, Botfield M, Tustison NJ, Leiva-Salinas C, et al. Use of hyperpolarized helium-3 MRI to assess response to ivacaftor treatment in patients with cystic fibrosis. *J Cyst Fibros*. 2017;16(2):267–74.
49. Chilla GS, Tan CH, Xu C, Poh CL. Diffusion weighted magnetic resonance imaging and its recent trend—a survey. *Quant Imaging Med Surg*. 2015;5(3):407–22.
50. Baliyan V, Das CJ, Sharma R, Gupta AK. Diffusion weighted imaging: technique and applications. *World J Radiol*. 2016;8(9):785–98.
51. van Beek EJ, Wild JM, Kauczor HU, Schreiber W, Mugler JP III, de Lange EE. Functional MRI of the lung using hyperpolarized 3-helium gas. *J Magn Reson Imaging*. 2004;20(4):540–54.
52. Saam BT, Yablonskiy DA, Kodibagkar VD, Leawoods JC, Gierada DS, Cooper JD, et al. MR imaging of diffusion of  $^3\text{He}$  gas in healthy and diseased lungs. *Magn Reson Med*. 2000;44(2):174–9.
53. Salerno M, Altes TA, Brookeman JR, de Lange EE, Mugler JP 3rd. Rapid hyperpolarized  $^3\text{He}$  diffusion MRI of healthy and emphysematous human lungs using an optimized interleaved-spiral pulse sequence. *J Magn Reson Imaging: JMRI*. 2003;17(5):581–8.
54. Wang C, Miller GW, Altes TA, de Lange EE, Cates GD Jr, Mugler JP 3rd. Time dependence of  $^3\text{He}$  diffusion in the human lung: measurement in the long-time regime using stimulated echoes. *Magn Reson Med*. 2006;56(2):296–309.
55. Diaz S, Casselbrant I, Piitulainen E, Magnusson P, Peterson B, Wollmer P, et al. Validity of apparent diffusion coefficient hyperpolarized  $^3\text{He}$ -MRI using MSCT and pulmonary function tests as references. *Eur J Radiol*. 2009;71(2):257–63.
56. Kirby M, Mathew L, Wheatley A, Santyr GE, McCormack DG, Parraga G. Chronic obstructive pulmonary disease: longitudinal hyperpolarized ( $^3\text{He}$ ) MR imaging. *Radiology*. 2010;256(1):280–9.
57. Chan H-F, Weatherley N, Johns CS, Stewart N, Collier G, Bianchi SM, et al. Airway microstructure in idiopathic pulmonary fibrosis: assessment at hyperpolarized  $^3\text{He}$  diffusion-weighted MRI. *Radiology*. 2019;291:181714.
58. Chan H-F, Stewart NJ, Parra-Robles J, Collier GJ, Wild JM. Whole lung morphometry with 3D multiple b-value hyperpolarized gas MRI and compressed sensing. *Magn Reson Med*. 2017;77(5):1916–25.
59. McCormack DG, Halko S, McKay S, Kirby M, Svenningsen S, Wheatley A, et al. Hyperpolarized  $^{129}\text{Xe}$  MRI feasibility, subject safety and tolerability: at the doorstep of clinical translation? In: A65 lung imaging: physiology and technology. American Thoracic Society; 2012. p. A2031-A.
60. Driehuys B, Martinez-Jimenez S, Cleveland ZI, Metz GM, Beaver DM, Nouls JC, et al. Chronic obstructive pulmonary disease: safety and tolerability of hyperpolarized  $^{129}\text{Xe}$  MR imaging in healthy volunteers and patients. *Radiology*. 2012;262(1):279–89.
61. Altes T, Mugler J, Dregely I, Ketel S, Ruset I, de Lange E, et al., editors. Hyperpolarized xenon-129 ventilation MRI: preliminary results in normal subjects and patients with lung disease. In: Proceedings 18th scientific meeting; 2010.
62. Kirby M, Svenningsen S, Owringi A, Wheatley A, Farag A, Ouriadov A, et al. Hyperpolarized  $^3\text{He}$  and  $^{129}\text{Xe}$  MR imaging in healthy volunteers and patients with chronic obstructive pulmonary disease. *Radiology*. 2012;265(2):600–10.
63. Svenningsen S, Kirby M, Starr D, Leary D, Wheatley A, Maksym GN, et al. Hyperpolarized ( $^3\text{He}$ ) and ( $^{129}\text{Xe}$ ) Xe MRI: differences in asthma before bronchodilation. *J Magn Reson Imaging: JMRI*. 2013;38(6):1521–30.
64. Costella S, Kirby M, Maksym GN, McCormack DG, Paterson NA, Parraga G. Regional pulmonary response to a methacholine challenge using

- hyperpolarized (3)He magnetic resonance imaging. *Respirology* (Carlton, VIC). 2012;17(8):1237–46.
65. Doganay O, Matin T, Chen M, Kim M, McIntyre A, McGowan DR, et al. Time-series hyperpolarized xenon-129 MRI of lobar lung ventilation of COPD in comparison to V/Q-SPECT/CT and CT. *Eur Radiol*. 2018;29:4058–67.
  66. He M, Driehuys B, Que LG, Huang YT. Using hyperpolarized (129)Xe MRI to quantify the pulmonary ventilation distribution. *Acad Radiol*. 2016;23(12):1521–31.
  67. Thomen RP, Walkup LL, Roach DJ, Cleveland ZI, Clancy JP, Woods JC. Hyperpolarized (129)Xe for investigation of mild cystic fibrosis lung disease in pediatric patients. *J Cyst Fibros*. 2017;16(2):275–82.
  68. Couch MJ, Thomen R, Kanhere N, Hu R, Ratjen F, Woods J, et al. A two-center analysis of hyperpolarized (129)Xe lung MRI in stable pediatric cystic fibrosis: potential as a biomarker for multi-site trials. *J Cyst Fibros*. 2019;18:728–33.
  69. Walkup LL, Roach DJ, Hall CS, Gupta N, Thomen RP, Cleveland ZI, et al. Cyst ventilation heterogeneity and alveolar airspace dilation as early disease markers in lymphangiomyomatosis. *Ann Am Thorac Soc*. 2019;16(8):1008–16.
  70. Kirby M, Svenningsen S, Kanhere N, Owrangi A, Wheatley A, Coxson HO, et al. Pulmonary ventilation visualized using hyperpolarized helium-3 and xenon-129 magnetic resonance imaging: differences in COPD and relationship to emphysema. *J Appl Physiol* (Bethesda, MD: 1985). 2013;114(6):707–15.
  71. Matin TN, Rahman N, Nickol AH, Chen M, Xu X, Stewart NJ, et al. Chronic obstructive pulmonary disease: lobar analysis with hyperpolarized (129)Xe MR imaging. *Radiology*. 2017;282(3):857–68.
  72. Thomen RP, Quirk JD, Roach D, Egan-Rojas T, Ruppert K, Yusen RD, et al. Direct comparison of (129) Xe diffusion measurements with quantitative histology in human lungs. *Magn Reson Med*. 2017;77(1):265–72.
  73. Walkup LL, Thomen RP, Akinyi TG, Watters E, Ruppert K, Clancy JP, et al. Feasibility, tolerability and safety of pediatric hyperpolarized (129)Xe magnetic resonance imaging in healthy volunteers and children with cystic fibrosis. *Pediatr Radiol*. 2016;46(12):1651–62.
  74. Kaushik SS, Freeman MS, Yoon SW, Liljereth MG, Stiles JV, Roos JE, et al. Measuring diffusion limitation with a perfusion-limited gas--hyperpolarized 129Xe gas-transfer spectroscopy in patients with idiopathic pulmonary fibrosis. *J Appl Physiol* (Bethesda, MD: 1985). 2014;117(6):577–85.
  75. Cleveland ZI, Cofer GP, Metz G, Beaver D, Nouis J, Kaushik SS, et al. Hyperpolarized Xe MR imaging of alveolar gas uptake in humans. *PLoS One*. 2010;5(8):e12192-e.
  76. Qing K, Shim Y, Tustison N, Altes T, Ruppert K, Mata J, et al. A19 getting polarized: MR imaging in obstructive lung disease: hyperpolarized xenon-129 MRI: a new tool to evaluate COPD. *Am J Respir Crit Care Med*. 2016;193:1.
  77. Qing K, Ruppert K, Jiang Y, Mata JF, Miller GW, Shim YM, et al. Regional mapping of gas uptake by blood and tissue in the human lung using hyperpolarized xenon-129 MRI. *J Magn Reson Imaging: JMRI*. 2014;39(2):346–59.
  78. Wang JM, Robertson SH, Wang Z, He M, Virgincar RS, Schrank GM, et al. Using hyperpolarized 129Xe MRI to quantify regional gas transfer in idiopathic pulmonary fibrosis. *Thorax*. 2018;73(1):21–8.
  79. Wang Z, He M, Bier E, Rankine L, Schrank G, Rajagopal S, et al. Hyperpolarized (129) Xe gas transfer MRI: the transition from 1.5T to 3T. *Magn Reson Med*. 2018;80(6):2374–83.
  80. Ohno Y, Hatabu H. Basics concepts and clinical applications of oxygen-enhanced MR imaging. *Eur J Radiol*. 2007;64(3):320–8.
  81. Loffler R, Muller CJ, Peller M, Penzkofer H, Deimling M, Schwaiblmair M, et al. Optimization and evaluation of the signal intensity change in multisection oxygen-enhanced MR lung imaging. *Magn Reson Med*. 2000;43(6):860–6.
  82. Mai VM, Liu B, Li W, Polzin J, Kurucay S, Chen Q, et al. Influence of oxygen flow rate on signal and T(1) changes in oxygen-enhanced ventilation imaging. *J Magn Reson Imaging: JMRI*. 2002;16(1):37–41.
  83. Oechsner M, Pracht ED, Staeb D, Arnold JF, Kostler H, Hahn D, et al. Lung imaging under free-breathing conditions. *Magn Reson Med*. 2009;61(3):723–7.
  84. Stadler A, Stiebellehner L, Jakob PM, Arnold JF, Eisenhuber E, von Katzler I, et al. Quantitative and o(2) enhanced MRI of the pathologic lung: findings in emphysema, fibrosis, and cystic fibrosis. *Int J Biomed Imaging*. 2007;2007:23624.
  85. Jobst BJ, Triphan SM, Sedlaczek O, Anjorin A, Kauczor HU, Biederer J, et al. Functional lung MRI in chronic obstructive pulmonary disease: comparison of T1 mapping, oxygen-enhanced T1 mapping and dynamic contrast enhanced perfusion. *PLoS One*. 2015;10(3):e0121520.
  86. Renne J, Lauer mann P, Hinrichs JB, Schonfeld C, Sorrentino S, Gutberlet M, et al. Chronic lung allograft dysfunction: oxygen-enhanced T1-mapping MR imaging of the lung. *Radiology*. 2015;276(1):266–73.
  87. Jakob PM, Wang T, Schultz G, Hebestreit H, Hebestreit A, Hahn D. Assessment of human pulmonary function using oxygen-enhanced T(1) imaging in patients with cystic fibrosis. *Magn Reson Med*. 2004;51(5):1009–16.
  88. Kaireit TF, Sorrentino SA, Renne J, Schoenfeld C, Voskrebenezov A, Gutberlet M, et al. Functional lung MRI for regional monitoring of patients with cystic fibrosis. *PLoS One*. 2017;12(12):e0187483.
  89. Ohno Y, Hatabu H, Takenaka D, Adachi S, Van Cauteren M, Sugimura K. Oxygen-enhanced MR ventilation imaging of the lung: preliminary clinical experience in 25 subjects. *AJR Am J Roentgenol*. 2001;177(1):185–94.

90. Ohno Y, Iwasawa T, Seo JB, Koyama H, Takahashi H, Oh Y-M, et al. Oxygen-enhanced magnetic resonance imaging versus computed tomography. *Am J Respir Crit Care Med*. 2008;177(10):1095–102.
91. Ohno Y, Koyama H, Matsumoto K, Onishi Y, Nogami M, Takenaka D, et al. Oxygen-enhanced MRI vs. quantitatively assessed thin-section CT: pulmonary functional loss assessment and clinical stage classification of asthmatics. *Eur J Radiol*. 2011;77(1):85–91.
92. Ohno Y, Nishio M, Koyama H, Yoshikawa T, Matsumoto S, Seki S, et al. Oxygen-enhanced MRI for patients with connective tissue diseases: comparison with thin-section CT of capability for pulmonary functional and disease severity assessment. *Eur J Radiol*. 2014;83(2):391–7.
93. Zha W, Nagle SK, Cadman RV, Schiebler ML, Fain SB. Three-dimensional isotropic functional imaging of cystic fibrosis using oxygen-enhanced MRI: comparison with hyperpolarized (3)He MRI. *Radiology*. 2019;290(1):229–37.
94. Renne J, Hinrichs J, Schonfeld C, Gutberlet M, Winkler C, Faulenbach C, et al. Noninvasive quantification of airway inflammation following segmental allergen challenge with functional MR imaging: a proof of concept study. *Radiology*. 2015;274(1):267–75.
95. Edelman RR, Hatabu H, Tadamura E, Li W, Prasad PV. Noninvasive assessment of regional ventilation in the human lung using oxygen-enhanced magnetic resonance imaging. *Nat Med*. 1996;2(11):1236–9.
96. Deibler AR, Pollock JM, Kraft RA, Tan H, Burdette JH, Maldjian JA. Arterial spin-labeling in routine clinical practice, part 1: technique and artifacts. *AJNR Am J Neuroradiol*. 2008;29(7):1228–34.
97. Mai VM, Bankier AA, Prasad PV, Li W, Storey P, Edelman RR, et al. MR ventilation-perfusion imaging of human lung using oxygen-enhanced and arterial spin labeling techniques. *J Magn Reson Imaging*: JMRI. 2001;14(5):574–9.
98. Bergin CJ, Pauly JM, Macovski A. Lung parenchyma: projection reconstruction MR imaging. *Radiology*. 1991;179(3):777–81.
99. Weiger M, Brunner DO, Dietrich BE, Muller CF, Pruessmann KP. ZTE imaging in humans. *Magn Reson Med*. 2013;70(2):328–32.
100. Miller GW, Mugler JP 3rd, Sá RC, Altes TA, Prisk GK, Hopkins SR. Advances in functional and structural imaging of the human lung using proton MRI. *NMR Biomed*. 2014;27(12):1542–56.
101. Tibiletti M, Paul J, Bianchi A, Wundrak S, Rottbauer W, Stiller D, et al. Multistage three-dimensional UTE lung imaging by image-based self-gating. *Magn Reson Med*. 2016;75(3):1324–32.
102. Higano NS, Hahn AD, Tkach JA, Cao X, Walkup LL, Thomen RP, et al. Retrospective respiratory self-gating and removal of bulk motion in pulmonary UTE MRI of neonates and adults. *Magn Reson Med*. 2017;77(3):1284–95.
103. Triphan SM, Breuer FA, Gensler D, Kauczor HU, Jakob PM. Oxygen enhanced lung MRI by simultaneous measurement of T1 and T2 \* during free breathing using ultrashort TE. *J Magn Reson Imaging*: JMRI. 2015;41(6):1708–14.
104. Higano N, Walkup L, Hahn A, Thomen R, Merhar S, Kingma P, et al., editors. Quantification of neonatal lung parenchymal density via ultra-short echo-time (UTE) magnetic resonance imaging (MRI). *American Journal of Respiratory and Critical Care Medicine*. New York: American Thoracic Society; 2016.
105. Higano NS, Spielberg DR, Fleck RJ, Schapiro AH, Walkup LL, Hahn AD, et al. Neonatal pulmonary magnetic resonance imaging of bronchopulmonary dysplasia predicts short-term clinical outcomes. *Am J Respir Crit Care Med*. 2018;198(10):1302–11.
106. Roach DJ, Cremillieux Y, Fleck RJ, Brody AS, Serai SD, Szczesniak RD, et al. Ultrashort echo-time magnetic resonance imaging is a sensitive method for the evaluation of early cystic fibrosis lung disease. *Ann Am Thorac Soc*. 2016;13(11):1923–31.
107. Dournes G, Menut F, Macey J, Fayon M, Chateil JF, Salel M, et al. Lung morphology assessment of cystic fibrosis using MRI with ultra-short echo time at submillimeter spatial resolution. *Eur Radiol*. 2016;26(11):3811–20.
108. Ma W, Sheikh K, Svenningsen S, Pike D, Guo F, Etamad-Rezai R, et al. Ultra-short echo-time pulmonary MRI: evaluation and reproducibility in COPD subjects with and without bronchiectasis. *J Magn Reson Imaging*: JMRI. 2015;41(5):1465–74.
109. Roach DJ, Cremillieux Y, Serai SD, Thomen RP, Wang H, Zou Y, et al. Morphological and quantitative evaluation of emphysema in chronic obstructive pulmonary disease patients: a comparative study of MRI with CT. *J Magn Reson Imaging*: JMRI. 2016;44(6):1656–63.
110. Chassagnon G, Martin C, Marini R, Vakalopolou M, Regent A, Mouthon L, et al. Use of elastic registration in pulmonary MRI for the assessment of pulmonary fibrosis in patients with systemic sclerosis. *Radiology*. 2019;291(2):487–92.
111. Burris NS, Johnson KM, Larson PE, Hope MD, Nagle SK, Behr SC, et al. Detection of small pulmonary nodules with ultrashort Echo time sequences in oncology patients by using a PET/MR system. *Radiology*. 2016;278(1):239–46.
112. Cha MJ, Park HJ, Paek MY, Stemmer A, Lee ES, Park SB, et al. Free-breathing ultrashort echo time lung magnetic resonance imaging using stack-of-spirals acquisition: a feasibility study in oncology patients. *Magn Reson Imaging*. 2018;51:137–43.
113. Wielputz MO, Lee HY, Koyama H, Yoshikawa T, Seki S, Kishida Y, et al. Morphologic characterization of pulmonary nodules with ultrashort TE MRI at 3T. *AJR Am J Roentgenol*. 2018;210(6):1216–25.
114. Sheikh K, Guo F, Capaldi DP, Ouriadov A, Eddy RL, Svenningsen S, et al. Ultrashort echo time MRI bio-

- markers of asthma. *J Magn Reson Imaging: JMIRI*. 2017;45(4):1204–15.
115. Willmering MM, Niedbalski PJ, Wang H, Walkup LL, Robison RK, Pipe JG, et al. Improved pulmonary (129) Xe ventilation imaging via 3D-spiral UTE MRI. *Magn Reson Med*. 2020;84(1):312–20.
  116. Kruger SJ, Fain SB, Johnson KM, Cadman RV, Nagle SK. Oxygen-enhanced 3D radial ultrashort echo time magnetic resonance imaging in the healthy human lung. *NMR Biomed*. 2014;27(12):1535–41.
  117. Ley S, Ley-Zaporozhan J, Pitton MB, Schneider J, Wirth GM, Mayer E, et al. Diagnostic performance of state-of-the-art imaging techniques for morphological assessment of vascular abnormalities in patients with chronic thromboembolic pulmonary hypertension (CTEPH). *Eur Radiol*. 2012;22(3):607–16.
  118. Stein PD, Chenevert TL, Fowler SE, Goodman LR, Gottschalk A, Hales CA, et al. Gadolinium-enhanced magnetic resonance angiography for pulmonary embolism: a multicenter prospective study (PIOPED III). *Ann Intern Med*. 2010;152(7):434–43.
  119. Schiebler ML, Nagle SK, François CJ, Replinger MD, Hamedani AG, Vigen KK, et al. Effectiveness of MR angiography for the primary diagnosis of acute pulmonary embolism: clinical outcomes at 3 months and 1 year. *J Magn Reson Imaging*. 2013;38(4):914–25.
  120. Yi CA, Lee KS, Han J, Chung MP, Chung MJ, Shin KM. 3-T MRI for differentiating inflammation- and fibrosis-predominant lesions of usual and nonspecific interstitial pneumonia: comparison study with pathologic correlation. *AJR Am J Roentgenol*. 2008;190(4):878–85.
  121. Maria Ta B, Andreas W, Christopher MR, Michael K, Claus Peter H, Mark K, et al. Contrast agent accumulation patterns in chronic interstitial lung disease using 5D MRI. *Br J Radiol*. 2020;93:20190121.
  122. Amaxopoulou C, Gnannt R, Higashigaito K, Jung A, Kellenberger CJ. Structural and perfusion magnetic resonance imaging of the lung in cystic fibrosis. *Pediatr Radiol*. 2018;48(2):165–75.
  123. Kellenberger CJ, Amaxopoulou C, Moehrlen U, Bode PK, Jung A, Geiger J. Structural and perfusion magnetic resonance imaging of congenital lung malformations. *Pediatr Radiol*. 2020;50:1083–94.
  124. Ohno Y, Fujisawa Y, Yui M, Takenaka D, Koyama H, Sugihara N, et al. Solitary pulmonary nodule: comparison of quantitative capability for differentiation and management among dynamic CE-perfusion MRI at 3 T system, dynamic CE-perfusion ADCT and FDG-PET/CT. *Eur J Radiol*. 2019;115:22–30.
  125. Horn M, Oechsner M, Gardarsdottir M, Köstler H, Müller MF. Dynamic contrast-enhanced MR imaging for differentiation of rounded atelectasis from neoplasm. *J Magn Reson Imaging*. 2010;31(6):1364–70.
  126. Wu W, Zhou S, Hippe DS, Liu H, Wang Y, Mayr NA, et al. Whole-lesion DCE-MRI intensity histogram analysis for diagnosis in patients with suspected lung cancer. *Acad Radiol*. 2020;28:e27–34.
  127. Huang Y-S, Chen JL-Y, Hsu F-M, Huang J-Y, Ko W-C, Chen Y-C, et al. Response assessment of stereotactic body radiation therapy using dynamic contrast-enhanced integrated MR-PET in non-small cell lung cancer patients. *J Magn Reson Imaging*. 2018;47(1):191–9.
  128. Xu J, Mei L, Liu L, Wang K, Zhou Z, Zheng J. Early assessment of response to chemotherapy in lung cancer using dynamic contrast-enhanced MRI: a proof-of-concept study. *Clin Radiol*. 2018;73(7):625–31.
  129. Bourjeily G, Pidas M, Khalil H, Rosene-Montella K, Rodger M. Pulmonary embolism in pregnancy. *Lancet*. 2010;375(9713):500–12.
  130. Rothblum-Oviatt C, Wright J, Lefton-Greif MA, McGrath-Morrow SA, Crawford TO, Lederman HM. Ataxia telangiectasia: a review. *Orphanet J Rare Dis*. 2016;11(1):159.
  131. Cullen SC, Gross EG. The anesthetic properties of xenon in animals and human beings, with additional observations on krypton. *Science (New York, NY)*. 1951;113(2942):580–2.
  132. Abdo WF, Heunks LMA. Oxygen-induced hypercapnia in COPD: myths and facts. *Crit Care*. 2012;16(5):323.
  133. Power SP, Moloney F, Twomey M, James K, O'Connor OJ, Maher MM. Computed tomography and patient risk: facts, perceptions and uncertainties. *World J Radiol*. 2016;8(12):902–15.
  134. Papi A, Brightling C, Pedersen SE, Reddel HK. Asthma. *Lancet*. 2018;391(10122):783–800.
  135. de Lange EE, Altes TA, Patrie JT, Gaare JD, Knake JJ, Mugler JP III, et al. Evaluation of asthma with hyperpolarized helium-3 MRI: correlation with clinical severity and spirometry. *Chest*. 2006;130(4):1055–62.
  136. Svenningsen S, Kirby M, Starr D, Coxson HO, Paterson NAM, McCormack DG, et al. What are ventilation defects in asthma? *Thorax*. 2014;69(1):63–71.
  137. Mirza S, Benzo R. Chronic obstructive pulmonary disease phenotypes: implications for care. *Mayo Clin Proc*. 2017;92(7):1104–12.
  138. Davey C, Zoumot Z, Jordan S, McNulty WH, Carr DH, Hind MD, et al. Bronchoscopic lung volume reduction with endobronchial valves for patients with heterogeneous emphysema and intact interlobar fissures (the BeLIVEr-HiFi study): a randomised controlled trial. *Lancet*. 2015;386(9998):1066–73.
  139. Eberhardt R, Herth FJF, Radhakrishnan S, Gompelmann D. Comparing clinical outcomes in upper versus lower lobe endobronchial valve treatment in severe emphysema. *Respiration*. 2015;90(4):314–20.
  140. Adams CJ, Capaldi DPI, Di Cesare R, McCormack DG, Parraga G. On the potential role of MRI biomarkers of COPD to guide bronchoscopic lung volume reduction. *Acad Radiol*. 2018;25(2):159–68.
  141. Kirby M, Mathew L, Heydarian M, Etamad-Rezai R, McCormack DG, Parraga G. Chronic obstructive pulmonary disease: quantification of bronchodilator

- effects by using hyperpolarized (3)He MR imaging. *Radiology*. 2011;261(1):283–92.
142. Kirby M, Pike D, Coxson HO, McCormack DG, Parraga G. Hyperpolarized 3He ventilation defects used to predict pulmonary exacerbations in mild to moderate chronic obstructive pulmonary disease. *Radiology*. 2014;273(3):887–96.
143. Horsley AR, Gustafsson PM, Macleod KA, Saunders C, Greening AP, Porteous DJ, et al. Lung clearance index is a sensitive, repeatable and practical measure of airways disease in adults with cystic fibrosis. *Thorax*. 2008;63(2):135–40.
144. Smith L, Marshall H, Aldag I, Horn F, Collier G, Hughes D, et al. Longitudinal assessment of children with mild cystic fibrosis using hyperpolarized gas lung magnetic resonance imaging and lung clearance index. *Am J Respir Crit Care Med*. 2018;197(3):397–400.
145. Martini K, Gyax CM, Benden C, Morgan AR, Parker GJM, Frauenfelder T. Volumetric dynamic oxygen-enhanced MRI (OE-MRI): comparison with CT Brody score and lung function in cystic fibrosis patients. *Eur Radiol*. 2018;28(10):4037–47.
146. Weatherley ND, Stewart NJ, Chan H-F, Austin M, Smith LJ, Collier G, et al. Hyperpolarised xenon magnetic resonance spectroscopy for the longitudinal assessment of changes in gas diffusion in IPF. *Thorax*. 2019;74(5):500–2.